

## Quasi-free scattering with ${}^6, {}^8\text{He}$ beams

L.V. Chulkov<sup>a,b,\*</sup>, F. Aksouh<sup>a,c</sup>, A. Bleile<sup>a</sup>, O.V. Bochkarev<sup>a,b</sup>,  
D. Cortina-Gil<sup>d</sup>, A.V. Dobrovolsky<sup>e</sup>, P. Egelhof<sup>a</sup>, H. Geissel<sup>a</sup>,  
M. Hellström<sup>a</sup>, N.B. Isaev<sup>e</sup>, O.A. Kiselev<sup>e,f</sup>, B.G. Komkov<sup>e</sup>,  
M. Matoš<sup>a</sup>, F.N. Moroz<sup>e</sup>, G. Münzenberg<sup>a</sup>, M. Mutterer<sup>g</sup>,  
V.A. Mylnikov<sup>e</sup>, S.R. Neumaier<sup>a</sup>, V.N. Pribora<sup>a,b</sup>,  
D.M. Seliverstov<sup>e</sup>, L.O. Sergeev<sup>e</sup>, A. Shrivastava<sup>h</sup>, K. Sümmerer<sup>a</sup>,  
S.Yu. Torilov<sup>i</sup>, H. Weick<sup>a</sup>, M. Winkler<sup>a</sup>, V.I. Yatsoura<sup>e</sup>

<sup>a</sup> Gesellschaft für Schwerionenforschung (GSI), D-64291 Darmstadt, Germany

<sup>b</sup> Kurchatov Institute, RU-123182 Moscow, Russia

<sup>c</sup> University of Leuven, B-3001 Leuven, Belgium

<sup>d</sup> Universidad Santiago de Compostela, E-15706 Santiago de Compostela, Spain

<sup>e</sup> Petersburg Nuclear Physics Institute, RU-188350 St. Petersburg, Russia

<sup>f</sup> Institut für Kernchemie, Universität Mainz, D-55099 Mainz, Germany

<sup>g</sup> Institut für Kernphysik, Technische Universität, D-64289 Darmstadt, Germany

<sup>h</sup> Bhabha Atomic Research Center, 400085 Mumbai, India

<sup>i</sup> St. Petersburg State University, RU-198904 St. Petersburg, Petrodvorets, Russia

Received 4 March 2005; received in revised form 29 April 2005; accepted 13 May 2005

Available online 8 June 2005

### Abstract

This paper presents the results of experimental investigations of  $(p, pn)$ ,  $(p, p\alpha)$  and  $(p, p{}^6\text{He})$  reactions with relativistic  ${}^6\text{He}$  and  ${}^8\text{He}$  beams impinging on a hydrogen target. Information on the structure of extremely neutron-rich nuclei was obtained by using the unique characteristic of quasi-free scattering processes and inverse kinematics. For the first time, momentum distributions of complex clusters inside  ${}^6\text{He}$  and  ${}^8\text{He}$  were measured. Spectroscopic factors for valence neutrons,  $\alpha$ - and  ${}^6\text{He}$  clusters were deduced from the experimental data. They demonstrate that the filling of the

\* Corresponding author.

E-mail address: [l.chulkov@gsi.de](mailto:l.chulkov@gsi.de) (L.V. Chulkov).

$p_{\frac{1}{2}}$  shell is the essential feature of the  $^8\text{He}$  structure. It is shown that the  $^8\text{He}$  cluster structure can be considered as a  $^6\text{He}$  core plus two valence neutrons.

© 2005 Elsevier B.V. All rights reserved.

PACS: 25.60.-t; 27.20.+n; 25.60.Gc; 21.60.Gx

Keywords: Drip-line nuclei  $^6,^8\text{He}$ ; Quasi-free scattering; Nuclear structure

## 1. Introduction

Studies of quasi-free scattering (QFS) reactions provide quite precise information concerning clustering effects in nuclei. In QFS, a probe particle scatters off a bound cluster inside a nucleus. The process leads to a separation of the cluster from the nucleus, the rest of the nucleus acts as a spectator. The transition amplitude may be separated into a reaction term and a nuclear structure term, this property is a prerequisite for nuclear-structure investigations.

Experimental investigations of QFS of the type  $(a, ax)$  with  $a, x = p, n, d, t, ^3\text{He}$  or  $\alpha$ , due to the simplicity of the reaction mechanism and due to the presence of three bodies in the final state is a unique and easy way to understand the nuclear structure. In the past, QFS studies have provided a wealth of nuclear structure information for stable nuclei [1–4]. The application of this method to experiments with radioactive beams is very promising. The QFS method has been used in investigations of the cluster structure of drip-line nuclei (for example, see Refs. [5,6] and references therein). However, these experiments were restricted mainly to the valence-neutron knockout by a complex particle ( $^9\text{Be}$  or  $^{12}\text{C}$ ). Moreover, the recoil nucleus and the knocked-out neutron usually were not detected in these experiments and relative contributions from the different reaction channels were not determined experimentally.

Here we present first investigations of valence-neutron and charged-cluster knockout from  $^6,^8\text{He}$  by protons making use of the specific kinematics of QFS. In order to disentangle different reaction channels, we propose an effective method based on reaction kinematics. The validity of the assumed QFS mechanism is proven by angular and energy correlations and by the dependence of the differential cross sections on the momentum transfer. The spectroscopic factors for valence neutrons,  $\alpha$  and  $^6\text{He}$  clusters, and the momentum distributions of knocked-out particles and of the spectators are among the main results of the present experiment.

The lighter isotope,  $^6\text{He}$ , a Borromean two-neutron halo system, has been studied in a large number of different experiments (see reviews [5,6]). Its structure is well understood and the ground state is to more than 90% a pure  $(0p_{3/2})^2$  state. The relatively simple structure of  $^6\text{He}$  makes it a bench-mark nucleus.  $^8\text{He}$  is an extreme example, thought to consist of an  $\alpha$ -core surrounded by a halo of four additional neutrons [7]. Besides, interactions of the valence neutrons with the core could also lead to configurations  $^6\text{He}(0^+) + 2n$  and  $^6\text{He}(2^+) + 2n$  [8,9].

The data obtained in this experiment agree well with the known features of the  $^6\text{He}$  structure, but indicate new and unexpected features of the  $^8\text{He}$  structure. The  $\alpha$ -particle

knockout from  $^8\text{He}$  is of special interest in connection with recently renewed discussions of a bound tetra-neutron nucleus [10].

## 2. Experiment

The experiment was performed at GSI, Darmstadt, where radioactive beams were produced by fragmentation of  $^{18}\text{O}$  (820 MeV/u and 730 MeV/u) beams from the heavy-ion synchrotron, SIS, on a  $8\text{ g/cm}^2$  beryllium production target. The secondary  $^{6,8}\text{He}$  beams with energies of 717 and 671 MeV/u, respectively, were selected by magnetic analysis in the fragment separator, FRS, and directed towards the reaction target which was placed in front of the large-gap magnetic dipole spectrometer, ALADIN. Beam intensities were  $1.9 \times 10^5$  1/s for  $^6\text{He}$  and  $1.6 \times 10^4$  1/s for  $^8\text{He}$ .

The divergence of the radioactive beams at the entrance of the experimental setup was about 3 mrad in horizontal and about 7 mrad in vertical direction, thus beam tracking was required. The experimental setup is displayed in Fig. 1.

The secondary beam passed first through energy-loss ( $\Delta E$ ) and time-of-flight (TOF) scintillators  $S_1$  and  $S_2$ . The direction of the beam particles was defined, with an angular resolution of  $\sigma_\vartheta = 0.08$  mrad, by two position-sensitive multi-wire proportional chambers, MWPC, (P1 and P2 in Fig. 1) placed at the entrance of the experimental cave and in front of the reaction target. The polar and azimuthal angles of reaction fragments were measured by two MWPC (P3 and P4 in Fig. 1). The achieved angular resolution ( $\approx 0.3$  mrad) was mainly determined by angular straggling in the target. The directions of the recoil protons were measured by two MWPC (P5 and P6 in Fig. 1) with an angular resolution of about 2 mrad.

Recoil protons emitted at polar angles larger than  $70^\circ$  with energies from 25 to 80 MeV were separated from background by the TOF and  $\Delta E$  technique. The proton energy

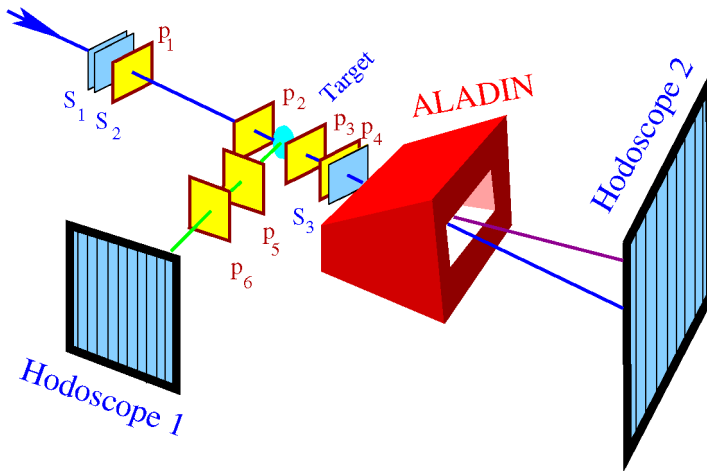


Fig. 1. Experimental set up.

was determined by the TOF method with a large position-sensitive scintillator wall (hodoscope 1) positioned at 2.3 m from the target. Hodoscope 1 consisted of two layers of vertical paddles (length  $\times$  width  $\times$  thickness = 110 cm  $\times$  5 cm  $\times$  1 cm). Each paddle of the second layer was shifted by 2.5 cm relative to the corresponding first-layer paddle.

Nuclear charges of the reaction fragments were determined from the energy losses in the scintillator  $S_3$ . Their isotopic composition was determined by analyzing their magnetic rigidity in ALADIN. The changes in their trajectories under the influence of the ALADIN field were measured with a position-sensitive scintillator wall (hodoscope 2) placed perpendicular to the beam direction 2.5 m downstream from the ALADIN exit.

The liquid-hydrogen target cell was mounted in a vacuum chamber with thin mylar windows. The effective thickness of the target was 708 mg/cm<sup>2</sup>. The target could be operated in an “empty mode” for background measurements.

The MWPC efficiencies ( $\epsilon_p$ ) calculated by a Monte Carlo simulation depend on the proton energy ( $T$ ). The  $\epsilon_p$  corrections are negligible at  $T \simeq 30$  MeV where  $\epsilon_p = 1.00 \pm 0.03$  while at  $T \simeq 80$  MeV the efficiency drops down to  $\epsilon_p = 0.26 \pm 0.04$  leading to a 15% systematic uncertainty in the data.

The invariant cross section  $\frac{d\sigma}{dt}$  as given in this article is defined as a function of the Lorentz-invariant Mandelstam variable  $t$  which corresponds to the square of the four-momentum transfer in QFS. The measured cross section was corrected for secondary nuclear reactions in the target.

The proton energies were determined by the TOF measurement. The time scale was calibrated by using the elastic-scattering events. The quality of this calibration was checked by comparing the elastic-scattering cross sections obtained from the angular distribution of

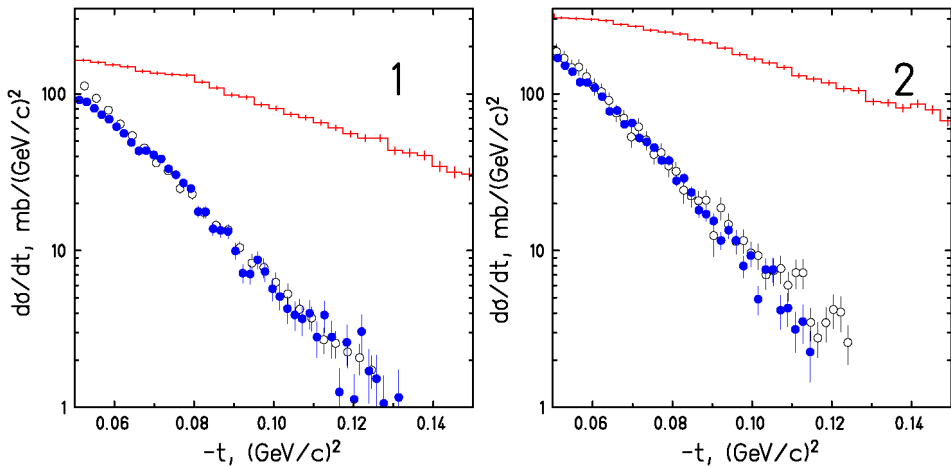


Fig. 2. Invariant cross-section for elastic and non-elastic scattering of  ${}^6\text{He}$  (panel 1) and  ${}^8\text{He}$  (panel 2) on the hydrogen target. The experimental data, obtained from the measured angular distribution of the scattered particles [11] are shown by open circles. The filled circles correspond to the cross section determined through the energy of the recoil protons. The histograms show the sum of the cross sections for all channels with  ${}^4\text{He}$  (for the  ${}^6\text{He}$  and  ${}^8\text{He}$  beams) and  ${}^6\text{He}$  (for the  ${}^8\text{He}$  beam only) fragments in the final state.

the ejectiles<sup>1</sup> with that from the energy distribution of the protons. The experimental cross sections are shown in Fig. 2 by open and closed circles with indication of the statistical uncertainties. Systematical errors arise from the accuracy of the beam monitor, of the target thickness, and of the proton detection efficiency. The uncertainties in the evaluation of the MWPC efficiencies are  $t$  dependent, thus the relative systematical uncertainty changes from about 5% at the lowest transferred momentum to about 20% at the highest.

The experimental results are presented in Section 4 in the form of different types of energy and angular correlations, of the transverse momentum distributions for the knocked-out clusters and for the spectators, and of the invariant cross sections for different reaction channels.

### 3. Basis for the data analysis

#### 3.1. Kinematics of quasi-free scattering

Consider a reaction in which a particle of mass  $m_0$  interacts with a nucleus of mass  $M_0$ , knocking out a particle of mass  $m_1$  and leaving behind a nucleus of mass  $M$ . The reaction is governed by four-momentum conservation

$$p_0 + P = Q + q_0 + q_1, \quad (1)$$

where  $p_0 = (\mathbf{p}_0, \omega_0)$  and  $q_0 = (\mathbf{q}_0, E_0)$  are the momenta of the probe before and after scattering, respectively.  $P = (\mathbf{P}, \omega_p)$  and  $Q = (\mathbf{Q}, E_Q)$  are the initial and final nuclear momenta, and  $q_1 = (\mathbf{q}_1, E_1)$  is the momentum of the cluster that is scattered off the nucleus. Fig. 3 presents a summary of the notations used in this paper. Further, all unprimed variables refer to the laboratory system ( $|\mathbf{p}_0| = 0$ , inverse kinematics), while all primed variables are used for the projectile center-of-mass (c.m.) system ( $|\mathbf{P}| = 0$ , conventional kinematics). The variables defined in the participant c.m. ( $|\mathbf{q}_0 + \mathbf{q}_1| = 0$ ) are marked by superscript cm.

In the impulse approximation, the reaction 1 proceeds via the exchange of a intermediate particle with momentum  $p_e = P - Q = q_0 + q_1 - p_0$ , as shown in the Feynman diagram with two vertices in Fig. 3. Momentum and energy conservation has to be fulfilled for each of the vertices. For the case of the neutron-rich helium isotopes we consider the knockout process as composed of different channels: knockout of a neutron or a cluster. The recoiled and knocked-out particles ( $q_0$  and  $q_1$ ) are participants and thus should reveal strong correlations. We consider first the correlations between the polar angles of participants. These correlations are to be similar to correlations between elastically scattered particles, but smoothed by the internal motion of the cluster inside the nucleus. The correlations between the azimuthal angles of the participants are expected to be very pro-

<sup>1</sup> The analysis of the elastic-scattering cross sections will be described in a separate paper, preliminary results on elastic scattering have been published in Ref. [11].

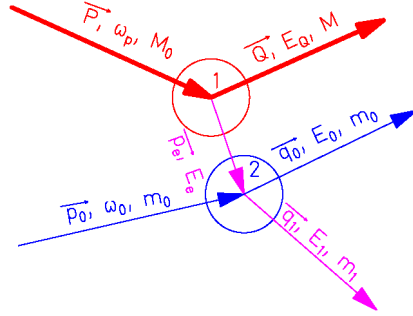


Fig. 3. Feynman diagram for quasi-free scattering in the impulse approximation and the notation used in the text. The vertex 1 corresponds to the reaction  $P \rightarrow Q + p_e$  with particles  $P$  and  $Q$  on the energy shell, while  $p_e$  is a virtual particle. The vertex 2 describes the reaction  $p_0 + p_e \rightarrow q_0 + q_1$  in which  $p_0$ ,  $q_0$ , and  $q_1$  have their physical masses.

nounced. In the laboratory system ( $|\mathbf{p}_0| = 0$ ), the angle between the momentum vector  $\mathbf{q}_1$  and  $\mathbf{q}_0 \times \mathbf{P}$ , which is perpendicular to the reaction plane,<sup>2</sup> is defined as follows:

$$\cos \theta = \frac{(\mathbf{q}_1 (\mathbf{q}_0 \times \mathbf{P}))}{|\mathbf{q}_1| |(\mathbf{q}_0 \times \mathbf{P})|} = \sin \vartheta_c \sin (\varphi_c - \varphi_p) = \frac{Q_{tr}}{|\mathbf{q}_1|}, \quad (2)$$

where  $Q_{tr}$  is a Cartesian component of the internal momentum of the cluster, perpendicular to the reaction plane,  $\vartheta_c$  is the polar angle of the knocked-out cluster, and  $\varphi_p$  and  $\varphi_c$  are the azimuthal angles for the recoil proton and the cluster, respectively. Momentum conservation ( $\mathbf{q}_0 + \mathbf{q}_1 = \mathbf{p}_e$ ) in the laboratory system ( $|\mathbf{p}_0| = 0$ ) at the vertex 2 of Fig. 3 was used to derive Eq. (2). The  $Q_{tr}$  value is significantly smaller than  $|\mathbf{q}_1|$ , thus the momenta of the knocked-out particles are aligned in the reaction plane ( $\theta \approx 90^\circ$ ).

### 3.2. Cross sections

The formulation of the impulse approximation in terms of relativistic variables was presented in Ref. [12]. This method was successfully used in the analysis of the experimental data of Ref. [13]. Further, we shall use the equation for the QFS cross section in the form which was given in Ref. [13], Eq. (3.4). The expression is given in terms of the three Lorentz scalars:

$$\begin{aligned} s &= (q_0 + q_1)^2, \\ u &= (P - Q)^2 = M_0^2 + M^2 - 2M_0 E'_Q, \\ t &= (p_0 - q_0)^2 = -2m_0 T, \end{aligned} \quad (3)$$

where  $s$ ,  $u$  and  $t$  characterize: the total energy of the  $q_0$ ,  $q_1$  subsystem, the internal momentum of the cluster and the momentum transferred in QFS, respectively.

The proposed method allows reducing the dependence of the QFS cross section from five to three parameters,  $s$ ,  $t$  and  $u$  [12,13]. One of the basic assumptions is that the two-

<sup>2</sup> The reaction plane is determined by the two vectors  $\mathbf{P}$  and  $\mathbf{q}_0$ .

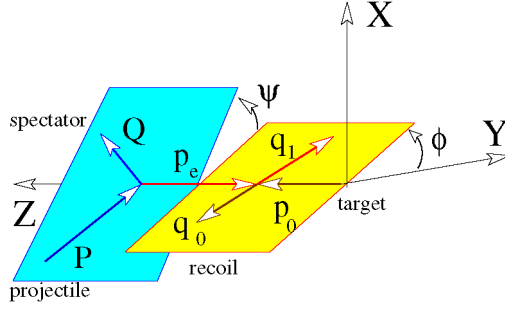


Fig. 4. Definition of the azimuthal angles  $\psi$  and  $\phi$  in the participant center-of-mass system  $\mathbf{q}_1 + \mathbf{q}_0 = 0$ . The Z axis is along  $\mathbf{p}_0^{\text{cm}}$  and therefore is different for each reaction event.

particle amplitude (vertex 2 in Fig. 3) can be evaluated with four legs on the energy shell. The cross section can then be factorized and written in the following form [13]:

$$d^5\sigma = S_c \frac{\sqrt{s} |\mathbf{q}^{\text{cm}}| E'_Q}{32\pi M_0 |\mathbf{p}_0| |\mathbf{q}'_0 + \mathbf{q}'_1| E'_e} \left( \frac{d\sigma}{dt} \right)_{pc} |\psi(Q')|^2 dt ds du d\phi d\psi, \\ |\mathbf{q}^{\text{cm}}|^2 = \frac{[s - (m_0 + m_1)^2][s - (m_0 - m_1)^2]}{4s}, \quad (4)$$

where  $\mathbf{q}^{\text{cm}}$  is the participant c.m. momentum;  $\phi$  and  $\psi$  are the azimuthal angles as defined in Fig. 4.

In the impulse approximation  $(\frac{d\sigma}{dt})_{pc}$  is properly a half-off-the-energy-shell cross section. The importance of off-energy-shell effects has been investigated in Refs. [4,14,15] with the example of the  $\alpha$ -knockout reaction  $(p, p'\alpha)$  on  $1p$ -shell nuclei. The conclusion is that off-energy-shell effects are small for tightly-bound clusters. The prescription is chosen to replace  $(\frac{d\sigma}{dt})_{pc}$  by a nearby measured on-energy-shell cross section, i.e., elastic scattering on a free cluster. The experimental elastic scattering  $p$ - $c$  cross section, measured at corresponding values of  $t$  and  $s$  can be used in the calculation. The other possibility is to replace  $(\frac{d\sigma}{dt})_{pc}$  by the elastic scattering cross section on a bound cluster. Usually for the tightly-bound clusters, the polarization effects are small and both approximations give similar results.

In the plane-wave impulse approximation (PWIA),  $|\psi(Q')|^2$  reduces to the momentum distribution of the cluster inside the nucleus. The distortion effects typically suppress the contribution of the nuclear interior and the knockout reaction is strongly localized at the surface. In PWIA, these effects are usually taken into account by introducing a lower radial cutoff.

The QFS cross section must be independent on the azimuthal angles  $\phi$  when the target is not polarized, as well as  $\psi$ -independent as a direct consequence of the impulse approximation. This was first proposed by Treiman and Yang [16] for a test of one-pion exchange, and then has been generalized for an arbitrary spin by Shapiro et al. [17]. Thus, the cross section depends essentially only on three variables:  $s$ ,  $t$  and  $u$ .

Furthermore, variations of  $s$  around the value determined by the beam energy influence mainly the kinematical term of Eq. (4). Thus, only two parameters are essential: the internal

momentum of the cluster described by  $u$ , and the momentum transferred to the proton in the scattering process described by  $t$ . Moreover, in the cases considered here, the integral over  $s$ ,  $u$ ,  $\phi$  and  $\psi$  results in a factor in front of the invariant cross section which is almost independent of  $t$  except for very small values of  $t$ :

$$\frac{d\sigma}{dt} = S_c \mathcal{F}(t) \left( \frac{d\sigma}{dt} \right)_{pc}. \quad (5)$$

In the case considered,  $\mathcal{F}(t)$  changes by less than 1% while  $t$  varies between 0.05 and 0.15 (GeV/c)<sup>2</sup>. The  $t$ -dependence of the QFS cross section is therefore an essential test of the proposed reaction mechanism.

### 3.3. Wave functions

The cluster spectroscopic factors were obtained by normalizing the solution of Eq. (5) to the experimental data. The cluster wave function (WF) was calculated with the prescription given in Ref. [3]. Since QFS is surface-peaked, the asymptotic form of the WF is expected to have the largest effect. As proper asymptotic WF we have chosen spherical Hankel functions

$$\psi(\mathbf{r}) = B h_l^{(1)}(i\beta r) Y_{lm}(\hat{r}), \quad r \geq R, \quad (6)$$

where  $\beta = \sqrt{2\mu\epsilon}$ ; here  $\mu$  is the reduced mass for the particles  $M$  and  $m_1$ , and  $\epsilon$  is the separation energy of  $m_1$  in  $M_0$ . The internal WF is given by

$$\psi(\mathbf{r}) = A j_l(\alpha r) Y_{lm}(\hat{r}), \quad r < R, \quad (7)$$

where  $j_l(\alpha r)$  and  $Y_{lm}(\hat{r})$  are spherical Bessel functions of the first kind and spherical harmonics, respectively. This WF corresponds to the solution of the Schrödinger equation for a square-well potential of radius  $R$ . The constants  $A$  and  $B$  are determined by requiring the continuity condition of  $\psi(\mathbf{r})$  at  $r = R$  and the normalization condition. The constant  $\alpha$  is fixed so that  $j_l(\alpha r)$  has the same number of nodes as required for the cluster WF. The parameter  $R$  was fixed by the requirement to have the root-mean-square radius of the valence neutron in  ${}^6\text{He}$  the same as was obtained in microscopic calculations ( $\langle r^2 \rangle = 4.8 \text{ fm}$ ) [18]. The depth of the well is determined by the binding energy of the cluster in the nucleus. The Fourier transform of the WF  $\psi(Q')$  was calculated with the cutoff parameter  $R_{\text{cut}}$  which was chosen to reproduce the  $\alpha$ -cluster momentum distribution in  ${}^6\text{He}$  (Fig. 10, panel 1). Note, that the wings of the distribution are not reproduced within this simple model. The reason is that in the high-momentum region the distribution is sensitive to the details of the WF at small radii; e.g., the agreement is better when a diffuse-edge cutoff function is used instead of a sharp cutoff radius. The parameters  $R = 3.5 \text{ fm}$  and  $R_{\text{cut}} = 2.5 \text{ fm}$  were kept the same in all calculations.



## 4. Experimental data

### 4.1. Reaction mechanism

In this section, we discuss how the features of the reaction mechanism have shown up in the experimental data. Published experimental data indicate that the QFS mechanism is the dominant process in the interaction of high-energy protons with nuclei [1]. However, a direct proof for the dominance of the quasi-free scattering is required as far as this assumption directly influences the results of the analysis.

A large probability for non-elastic processes is the first fact which has to be mentioned. Non-elastic cross sections—presented in Fig. 2 by the histograms—include all channels with  $^4\text{He}$  (for the  $^6\text{He}$  and  $^8\text{He}$  beams) and  $^6\text{He}$  (for the  $^8\text{He}$  beam only) in the final state. The magnitude of the non-elastic cross sections is significantly larger than that of the elastic scattering. This fact cannot be explained as the excitation and decay of isolated resonances in  $^6,8\text{He}$ : from eikonal calculations, the corresponding cross sections are estimated to be smaller by about two orders of magnitude. Thus large non-elastic cross section is a first indication of a dominance of QFS.

#### 4.1.1. Angular and energy correlations

The correlations between polar angles  $\vartheta_p$  and  $\vartheta_\alpha$  and between azimuthal angles  $\varphi_p$  and  $\varphi_\alpha$  are shown in Fig. 5 (panel 1 and panel 2, respectively) for the fragmentation of the 717 MeV/u  $^6\text{He}$  beam and detection of a proton in coincidence with  $^4\text{He}$ . The correlations between polar angles  $\vartheta_p$  and  $\vartheta_\alpha$  shown in Fig. 5 (panel 1) are characterized by events concentrated in two separate groups. In the lower group ( $A_\vartheta$ ) correlations are not pronounced, while strong correlations can be observed in the upper group ( $B_\vartheta$ ). The correlations between azimuthal angles  $\varphi_p$  and  $\varphi_\alpha$  in Fig. 5 (panel 2) reveal as well two groups of events. The first group ( $A_\varphi$ ) is characterized by a uniform distribution on azimuthal angles, while

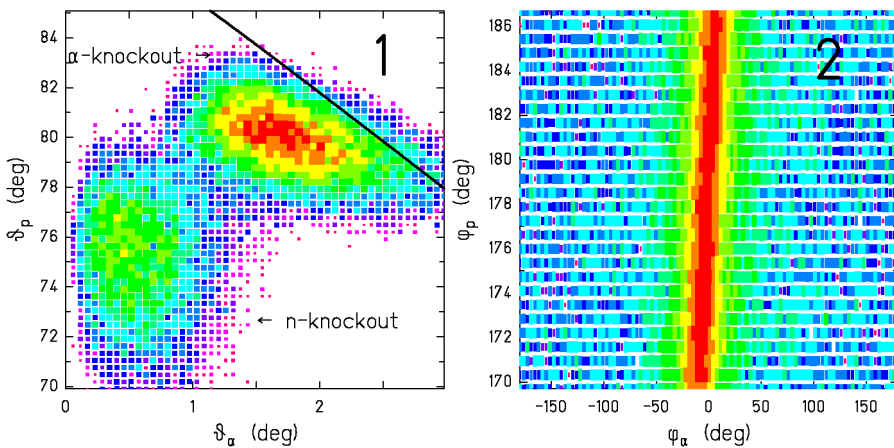


Fig. 5. Correlations between angles of the recoil protons and the  $\alpha$ -particles in the  $^1\text{H} + ^6\text{He}$  reaction. The polar angles  $\vartheta_p$ ,  $\vartheta_\alpha$  (panel 1) and azimuthal angles  $\varphi_p$ ,  $\varphi_\alpha$  (panel 2) are defined relative to the beam direction in the laboratory frame.

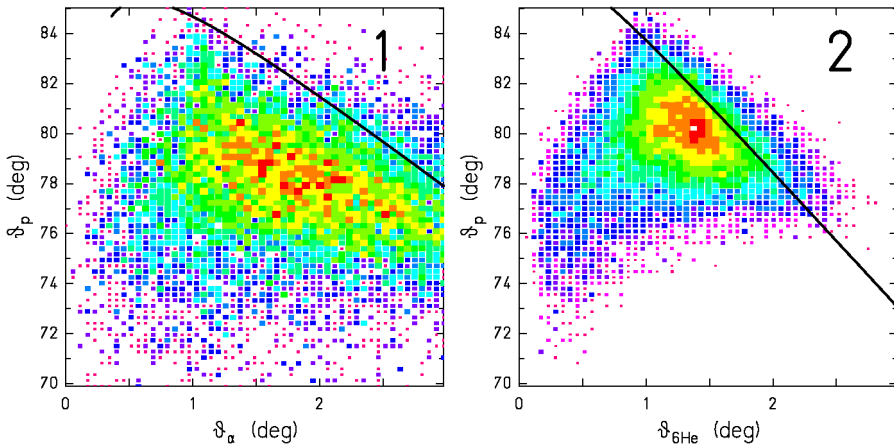


Fig. 6. Correlations between polar angles of the recoil proton and the  $\alpha$ -particle (panel 1) and between polar angles of the recoil proton and  ${}^6\text{He}$  (panel 2) in the  ${}^1\text{H} + {}^8\text{He}$  reaction. The polar angles  $\vartheta_p$ ,  $\vartheta_\alpha$  and  $\vartheta_{{}^6\text{He}}$  are defined relative to the beam direction in the laboratory system. Only events with  $170^\circ \leq \varphi_p - \varphi_\alpha \leq 190^\circ$  are shown.

events from the second group ( $B_\varphi$ ) are concentrated at  $\varphi_p - \varphi_\alpha \approx 180^\circ$ . The straightforward correspondence was observed between these groups: the events from group  $A_\vartheta$  also belong to group  $A_\varphi$ , while group  $B_\vartheta$  contains mainly events from group  $B_\varphi$ . This can be interpreted assuming that the  $A_\vartheta$  ( $A_\varphi$ ) events correspond to the channel where neutron knockout dominates and the  $\alpha$ -particles are spectators. The neutron knockout results in unstable  ${}^5\text{He}$  which then decays by neutron emission. In the  $B_\vartheta$  ( $B_\varphi$ ) group, the  $\alpha$ -particles are participants and these events correspond to the  $\alpha$  knockout channel. Distributions with similar features were obtained with the  ${}^8\text{He}$  beam when the recoil protons were detected in coincidence either with  ${}^4\text{He}$  or with  ${}^6\text{He}$ .

Fig. 6 presents experimental data obtained with the  ${}^8\text{He}$  beam. In order to emphasize the correlations between polar angles, only events with the momentum aligned in the reaction plane were selected. Panel 1 of Fig. 6 displays the distribution corresponding to the coincidence between proton and  $\alpha$ -particle. The case with  ${}^6\text{He}$  in the final state is shown in panel 2. These correlations are similar to those obtained for the case of the  ${}^6\text{He}$  beam. The solid lines in Figs. 5 and 6 show the results of kinematical calculations for a proton scattering off a bound cluster. The internal momentum of the cluster was set to zero and the residual system ( $2n$  in the case of  $\alpha$ -knockout from  ${}^6\text{He}$  and of  ${}^6\text{He}$ -knockout from  ${}^8\text{He}$ ,  $4n$  in the case of  $\alpha$ -knockout from  ${}^8\text{He}$ ) was assumed to be in its lowest energy state, i.e., the kinetic energies of the particles in their center-of-mass system were set to zero. The calculations reproduce the trends in the dependence of  $\vartheta_p$  versus  $\vartheta_\alpha$  but are shifted by about  $0.5$ – $1^\circ$  in  $\vartheta_\alpha$ . Note that the internal momentum of the cluster results in a spread in the  $\vartheta_p$  versus  $\vartheta_\alpha$  dependence and in a shift towards smaller angles.

Another check of the kinematical relations for QFS can be done by using the measured dependence of  $\vartheta_p$  on  $T$ . The distributions obtained for the proton quasi-free scattering on the valence neutron and on the  $\alpha$ -cluster in  ${}^6\text{He}$  are shown in Fig. 7.

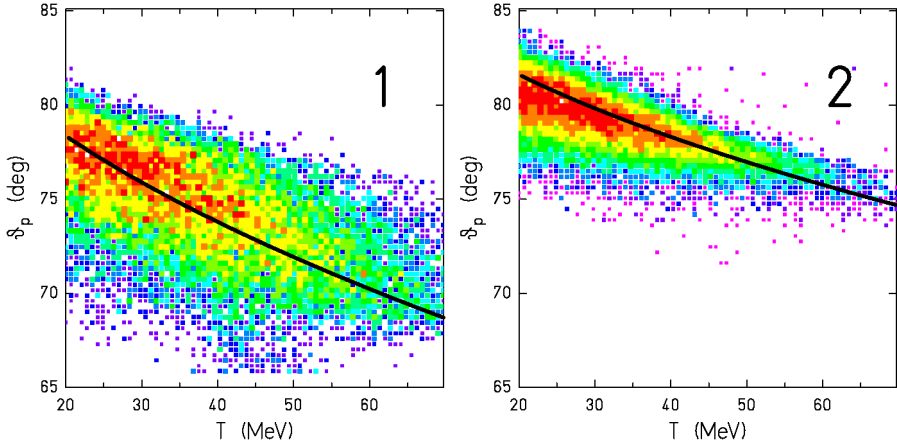


Fig. 7. (1) Correlations between the recoil-proton angle and its energy for the neutron-knockout channel in the  $^1\text{H} + ^6\text{He}$  reaction. The solid curve presents the calculations assuming a quasi-free neutron knockout  $^1\text{H}(^6\text{He}, pn)^5\text{He}$ . The neutron momentum inside  $^6\text{He}$  was set to zero. (2) Correlations between the recoil-proton angle and its energy for the  $\alpha$ -knockout channel in the  $^1\text{H} + ^6\text{He}$  reaction. The solid curve shows the calculation assuming an  $\alpha$  knockout  $^1\text{H}(^6\text{He}, p\alpha)2n$  with the relative energy between the neutrons equal to 0. The internal momentum of the  $\alpha$ -cluster was set to zero.

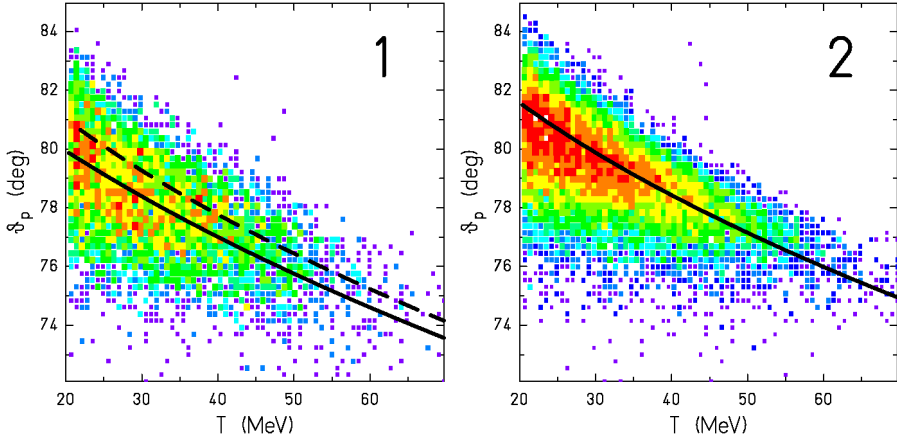


Fig. 8. (1) Correlations between the recoil proton angle and its energy for the  $\alpha$ -knockout channel in the  $^1\text{H} + ^8\text{He}$  reaction. The dashed curve is the result of calculations assuming a quasi-free  $\alpha$ -knockout leaving four neutrons with zero internal energy. The solid curve presents the same calculations but the total kinetic energy in the four-neutron system was set to 5 MeV. The internal momentum of the  $\alpha$ -cluster was set to zero. (2) Correlations between the recoil proton angle and its energy for the  $^6\text{He}$ -knockout channel in the  $^1\text{H} + ^8\text{He}$  reaction. The solid curve is the result of calculations assuming a quasi-free knockout of  $^6\text{He}$  leaving two neutrons with zero relative energy. The internal momentum of the  $^6\text{He}$ -cluster was set to zero.

The solid lines in panel 1 of the figure show the kinematical dependence of  $\vartheta_p(T)$  assuming neutron knockout by a proton resulting in  $^5\text{He}$  in its ground state. The internal momentum of the neutron was assumed to be zero. Similar calculations made for a quasi-

free  $\alpha$  knockout are shown in panel 2 of Fig. 7. The corresponding results obtained with the  $^8\text{He}$  beam are presented in Fig. 8. In the case of  $^8\text{He}$ , knockout of an  $\alpha$ -particle leads to four neutrons in the final state. The dashed line in Fig. 8 (panel 1) shows the calculation where the separation energy of the  $\alpha$ -particle was set to 3.11 MeV, equivalent to the total kinetic energy of four neutrons in their c.m. system being equal to zero. Better agreement with the data is achieved when the separation energy is set to 8 MeV. The calculation for the  $^6\text{He}$  knockout leading to two neutrons with zero relative energy shown in Fig. 8 (panel 2) are in agreement with the experimental distribution.

#### 4.1.2. Momentum distributions of spectators

We now come to the lower group defined in the distribution shown in Fig. 5. As was discussed above, these events correspond to the quasi-free neutron knockout. The rest of the nucleus is unstable and decays via neutron emission. The experimental data allow to reconstruct the transverse momentum distributions of these decay products,  $p_x = P_b \cos \vartheta_c \cos \varphi_c$ , where  $P_b$  is the momentum of a fragment moving with beam velocity. The transverse momentum distributions of the detected  $\alpha$  and  $^6\text{He}$  obtained with the  $^6\text{He}$  and  $^8\text{He}$  beams are shown in Fig. 9.

The momentum distributions of the spectators are determined by the internal structure of the nucleus and thus the measured distributions should not show any dependence on beam energy or on the type of the probe particle  $p_0$ . This independence is demonstrated in Fig. 9 where the momentum distributions from the present experiment are compared with the results obtained with 240 MeV/u  $^6\text{He}$  and 227 MeV/u  $^8\text{He}$  beams interacting with a carbon target [19].

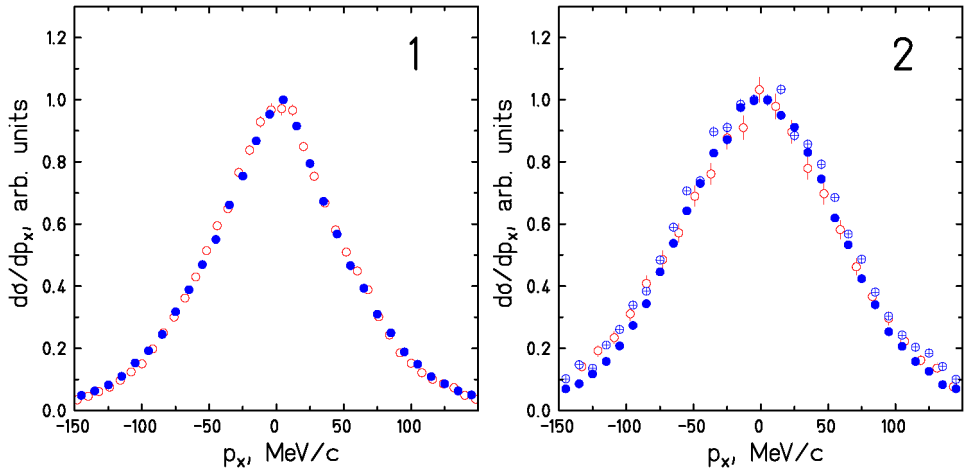


Fig. 9. Transverse momentum distributions of spectators resulting from neutron knockout process. (1)  $\alpha$ -spectator originating from  $^6\text{He}$  projectile. The experimental data of the present experiment are shown by filled circles (FWHM =  $102 \pm 5$  MeV/c). The data obtained with a 240 MeV/u  $^6\text{He}$  beam impinging on a carbon target [19] are shown by open circles. (2)  $^6\text{He}$ -spectator (filled circles, FWHM =  $135 \pm 5$  MeV/c) and  $^4\text{He}$ -spectator (circles with a cross, FWHM =  $143 \pm 5$  MeV/c) originating from  $^8\text{He}$  projectile. Open circles correspond to the interaction of a 227 MeV/u  $^8\text{He}$  beam with a carbon target resulting in  $\alpha$ -fragments [19].

Note, that for  $^8\text{He}$  the widths are nearly the same in the neutron-knockout channels:  $\text{FWHM} = 135 \pm 5 \text{ MeV}/c$  in  $^8\text{He}(p, pn\alpha)$  and  $\text{FWHM} = 143 \pm 5 \text{ MeV}/c$  in  $^8\text{He}(p, pn\ ^6\text{He})$ . This finding is interpreted as due to the fact that the width of the momentum distribution is determined to a large extent by the internal-momentum distribution of a valence neutron in  $^8\text{He}$ .

#### 4.1.3. Conclusion on the reaction mechanism

Conclusion on the dominant contribution of QFS mechanism to the measured yield in the interaction of  $^6\text{He}$  and  $^8\text{He}$  with a hydrogen target is based on the following evidences:

- Large cross sections for the inelastic channels.
- Observed correlations between polar angles of the recoil protons and the knocked-out particles, and between their azimuthal angles.
- The measured dependence of the proton energy  $T$  on the polar angle  $\vartheta_p$  is reproduced by the QFS kinematics.
- The measured transverse-momentum distributions of the fragments in channels associated with neutron knockout do not depend neither on the type of the target nor on the beam energy.

The crucial point is the dependence of  $\frac{d\sigma(t)}{dt}$  on  $t$ . In QFS, the dependence should be similar to that for the elastic scattering on a free cluster.

In the next two sections, a comprehensive analysis of the invariant cross sections in the different channels of QFS will be done. Since the structure of  $^6\text{He}$  is comparatively simple and has been studied carefully in series of experiments and in theoretical calculations, we shall use the results obtained with the  $^6\text{He}$  beam as benchmark data to check the applicability of different assumptions and as a test of the model which will then be used to calculate spectroscopic factors for different cluster configurations in  $^8\text{He}$ .

#### 4.2. Internal momentum distribution of the $^4,^6\text{He}$ clusters

The transverse momentum distributions of the spectators were shown in Fig. 9 and discussed above. In this case, the detected fragments are decay products of the spectators ( $^5\text{He}$  or  $^7\text{He}^*$ ) and their momenta are related to the valence neutron momenta inside the nucleus but distorted by the final-state interaction between the neutron and the fragment. In contrast, no experimental information was published up to date about internal momenta of complex clusters in the Borromean nuclei  $^6,^8\text{He}$ .

The transverse internal momentum distribution of a cluster inside the projectile  $\frac{d\sigma}{dQ_{\text{tr}}}$  can be directly obtained from data on the cluster-knockout channels using Eq. (2) and assumption that  $q_1 \approx P_b$ . This assumption is valid within an accuracy of a few percent

$$\frac{d\sigma}{dQ_{\text{tr}}} = \frac{1}{P_b \sin \theta} \frac{d\sigma}{d\theta}. \quad (8)$$

The resulting transverse momentum distributions are displayed in Fig. 10. The width of  $\frac{d\sigma}{dQ_{\text{tr}}}$  in the  $^6\text{He}(p, \alpha)$  and  $^8\text{He}(p, ^6\text{He})$  are nearly the same: in the  $\alpha$ -knockout  $\text{FWHM} = 75 \pm 5 \text{ MeV}/c$ , while in the  $^6\text{He}$  knockout  $\text{FWHM} = 82 \pm 5 \text{ MeV}/c$ . The width of the dis-

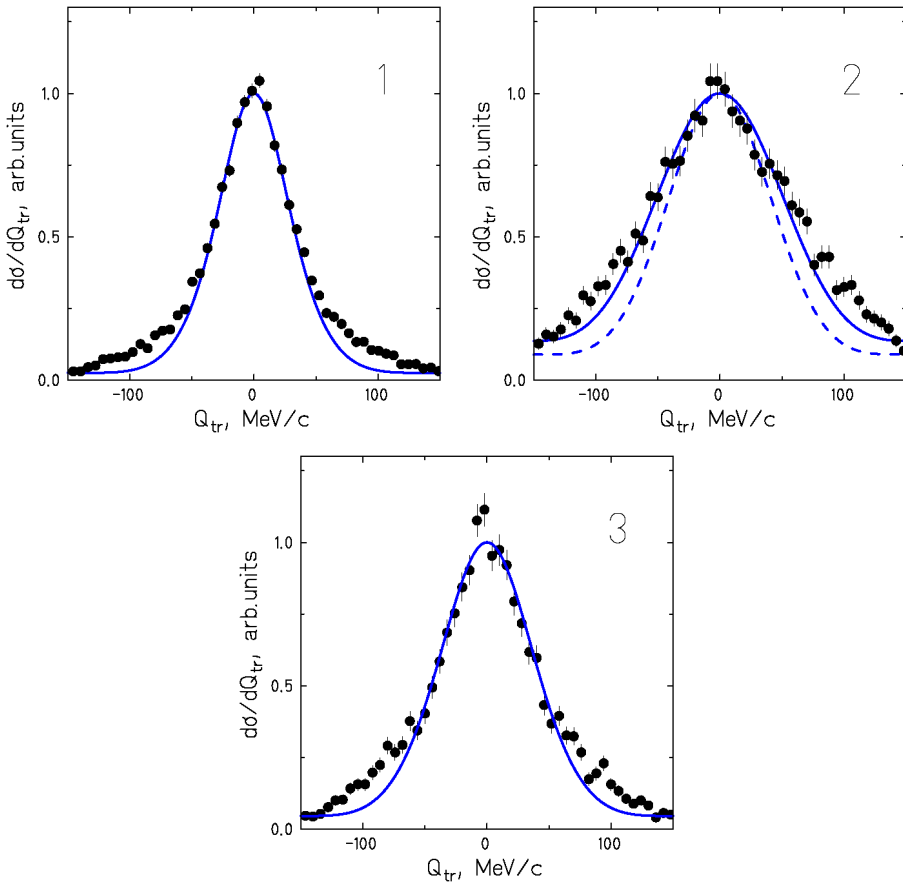


Fig. 10. Transverse momentum distributions of complex clusters from the cluster-knockout channels. The experimental data of the present experiment are shown by filled circles. (1) knocked out  $\alpha$ -cluster resulting from  ${}^6\text{He}$ ,  $\text{FWHM} = 75 \pm 5 \text{ MeV}/c$ . (2) knocked out  $\alpha$ -cluster resulting from  ${}^8\text{He}$ ,  $\text{FWHM} = 134 \pm 5 \text{ MeV}/c$ . (3) knocked out  ${}^6\text{He}$ -cluster resulting from  ${}^8\text{He}$ ,  $\text{FWHM} = 82 \pm 5 \text{ MeV}/c$ . Solid and dotted lines are the results of model calculation (see text for explanations).

tribution is significantly broader in the  $\alpha$ -knockout from  ${}^8\text{He}$ ,  $\text{FWHM} = 134 \pm 5 \text{ MeV}/c$ . Experimental resolution ( $\sigma = 12 \text{ MeV}/c$ ) does not influence significantly on the shape of the measured distributions. In Fig. 10, the experimental points are compared with the PWIA calculation. Details of the calculation are given in Section 3.3. The solid lines in panels 1 and 3 represent the expected internal momentum distributions of  $\alpha$ -clusters in  ${}^6\text{He}$  or  ${}^6\text{He}$ -clusters in  ${}^8\text{He}$ . The dotted line in panel 2 has been obtained with an  $\alpha$ -particle separation energy of 3.11 MeV. The solid line which is much closer to the experimental distribution was calculated assuming a value of 8 MeV for the  $\alpha$ -particle separation energy. The same result was obtained in Section 4.1.1 in the analysis of the  $\vartheta_p$  versus  $T$  dependence. This value indicates either the existence of a resonance at 5 MeV in the tetra-

neutron system or reflects strong internal correlations of the four neutrons in the  ${}^8\text{He}$  wave function.

#### 4.3. Cross sections

The invariant cross sections for different reaction channels are presented in Figs. 11–13. The QFS cross sections are shown in comparison with the corresponding free elastic-scattering data normalized to the values of the measured cross sections. The  $t$  dependence of the  $\alpha$ -particle knockout cross section and the experimental data for  ${}^4\text{He}(p, p)$  elastic scattering obtained at 800 MeV/u [20], close to the incident energy of the present experiment, are shown in Fig. 11. The experimental  ${}^4\text{He}(p, p)$  elastic scattering data are shown by open circles with an indication of error bars. The solid line drawn through these data results from a fit of an exponential function to the elastic data. The parameters of the fit are given in Ref. [20]. The same function is shown in Fig. 13 for the quasi-free  $\alpha$  knockout in the reaction with the  ${}^8\text{He}$  beam. In all the cases which are demonstrated in Figs. 11 (panels 1 and 2), 12 (panels 1 and 2) and 13 (panel 1) the invariant cross sections for QFS and for elastic scattering show similar  $t$ -dependence which confirms the dominance of the QFS mechanism.

However, the distribution which can correspond to the knockout of the  ${}^6\text{He}$  cluster does not show the expected behavior as seen in Fig. 13 (panel 2). The  $t$ -dependence of the present  $\frac{d\sigma}{dt}$  is more flat than for the  ${}^6\text{He}-p$  elastic scattering. The calculations for inelastic scattering with excitation of the  $2^+$  state in  ${}^8\text{He}$  in the eikonal Born approximation

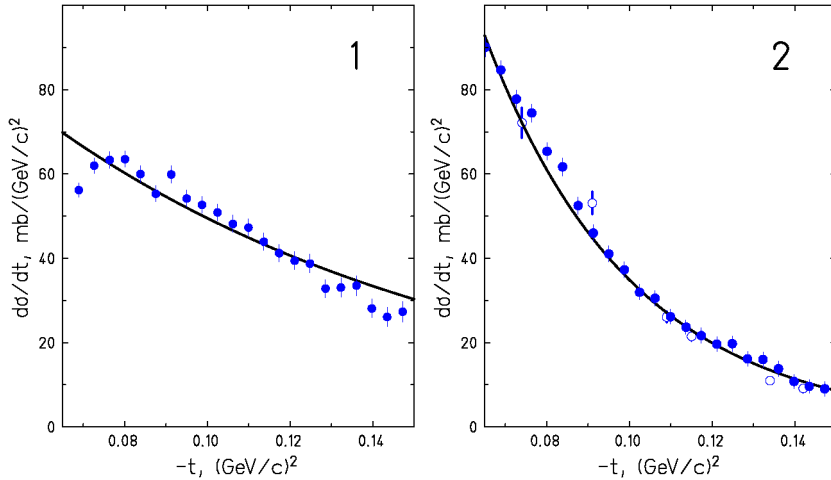


Fig. 11. (1) Invariant cross section for neutron knockout  ${}^6\text{He}(p, pn)$ . The solid line shows the free  $p$ - $n$  elastic-scattering cross section, normalized to the experimental data. (2) Invariant cross section for  $\alpha$ -knockout  ${}^6\text{He}(p, p\alpha)$ . Experimental data for  $p$ - $\alpha$  elastic scattering cross sections at 800 MeV [20] are shown by open circles. The solid line represents a fit of an exponential function to these data. The elastic cross sections are normalized to the quasi-free scattering data.

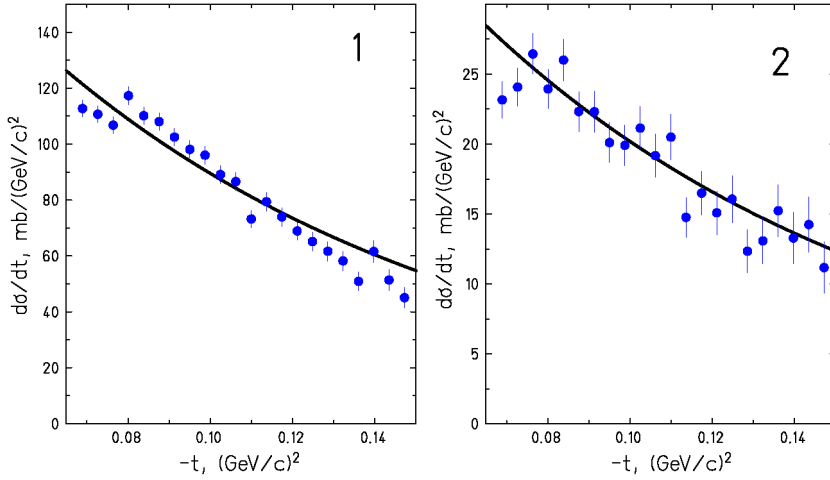


Fig. 12. Invariant cross-section for neutron knockout  ${}^8\text{He}(p, pn)$ . (1)  ${}^6\text{He}$  fragment in the final state. (2)  ${}^4\text{He}$  fragment in the final state. The solid line shows free  $p$ - $n$  elastic scattering cross sections, normalized to the experimental data.

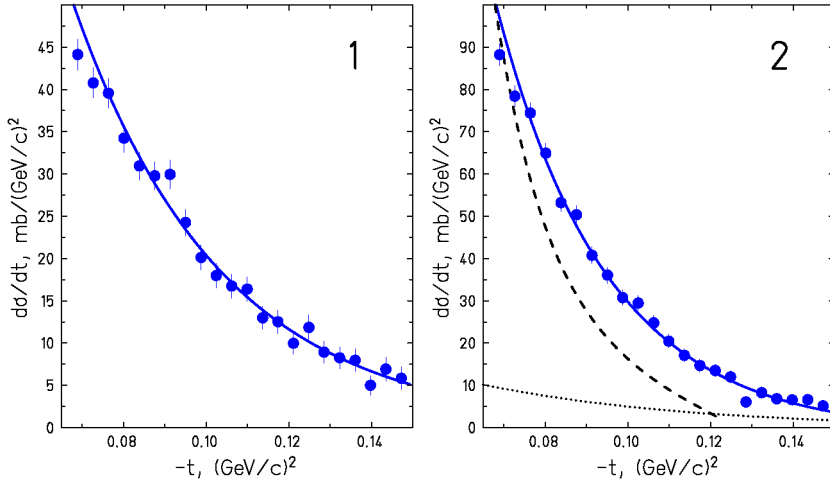


Fig. 13. (1) Invariant cross-section for  $\alpha$ -knockout  ${}^8\text{He}(p, p\alpha)$ . The solid line shows the free  $p$ - $\alpha$  elastic scattering cross section, normalized to the experimental data. (2) Invariant cross-section which could be associated with the  ${}^6\text{He}$ -knockout channel  ${}^8\text{He}(p, p{}^6\text{He})$ . The  $p$ - ${}^6\text{He}$  elastic scattering cross section [11], normalized to the experimental data at low  $|t|$ , is shown by the dashed line. The solid line represents the expected elastic scattering cross section on the  ${}^6\text{He}$  cluster with  $\langle r^2 \rangle^{1/2} = 1.8$  fm. The dotted line displays the result of DWBA calculations for the excitation of the  ${}^8\text{He}$   $2^+$  state.

(DWBA) [21] are shown in Fig. 13 (2) by dotted line.<sup>3</sup> The contribution from this chan-

<sup>3</sup> These calculations were previously checked by reproducing the proton inelastic scattering data at 72 MeV/u [22] where this process dominates in the  ${}^8\text{He}(p, p{}^6\text{He})$  channel.



Table 1  
Spectroscopic factors for different cluster configurations in  ${}^6\text{He}$  and  ${}^8\text{He}$

Projectile	Knocked out particle	Final state	$S_c$ experimental	$S_c$ shell model
${}^6\text{He}$	$n$	$p + 2n + \alpha$	1.7(2)	2
${}^6\text{He}$	$\alpha$	$p + 2n + \alpha$	0.8(1) <sup>a</sup>	1
${}^8\text{He}$	$n$	$p + 4n + \alpha$	0.8(1)	0
${}^8\text{He}$	$n$	$p + 2n + {}^6\text{He}$	3.3(3)	4
${}^8\text{He}$	$\alpha$	$p + 4n + \alpha$	0.9(1)	1
${}^8\text{He}$	${}^6\text{He}$	$p + 2n + {}^6\text{He}$	1.3(1) <sup>a,b</sup>	$\frac{1}{6}$

<sup>a</sup> Corrected for the contribution from the inelastic scattering.

<sup>b</sup> Obtained with  $\frac{d\sigma}{dt}$  calculated for the  ${}^6\text{He}$ -cluster matter radius  $\langle r^2 \rangle^{1/2} = 1.8$  fm.

nel is small and cannot explain the observed  $t$ -dependence. In this case it seems that the replacement of the half-off-the-shell cross section by the on-the-shell cross section is not a good approximation for the loosely bound  ${}^6\text{He}$  cluster. We come back to this problem in Section 4.4.

#### 4.4. Discussion of spectroscopic factors

The data shown in Figs. 11, 12 and 13 (panel 1) are used to obtain the corresponding spectroscopic factors utilizing Eq. (4). The deduced cluster spectroscopic factors ( $S_c$ ) are presented in Table 1. Indicated uncertainties are connected with statistical fluctuations and with the accuracy of the absolute normalization of the measured cross section. The spectroscopic factors  $S_n = 1.7(2)$  and  $S_\alpha = 0.8(1)$  obtained with the  ${}^6\text{He}$  beam are in agreement with the expected  ${}^6\text{He}$  structure: an  $\alpha$ -core surrounded by two neutrons. This confirms the validity of the approximations used in the analysis.

The main aim of the present investigation is to clarify the cluster-structure of  ${}^8\text{He}$ . The sum of two spectroscopic factors obtained in neutron-knockout channels  ${}^8\text{He}(p, pn\alpha)$  and  ${}^8\text{He}(p, pn {}^6\text{He})$ ,  $S_n^\alpha + S_n^{6\text{He}} = 4.1(3)$ , together with the spectroscopic factor deduced in the  $\alpha$ -knockout channel  ${}^8\text{He}(p, p\alpha)$ ,  $S_\alpha = 0.9(1)$ , confirm that the  ${}^8\text{He}$  structure is mainly an  $\alpha$ -core surrounded by a halo of four neutrons. The question is: could the neutrons be grouped in a way to form a  ${}^6\text{He} + 2n$  structure inside  ${}^8\text{He}$ ?

In the existing  $\alpha + 4n$  models of  ${}^8\text{He}$  [8,23,24], an assumption has been made that the population of the  $0p_{1/2}$ -orbit can be neglected and, thus,  ${}^8\text{He}$  is a nucleus with a closed  $0p_{3/2}$ -shell. This assumption implies significant restrictions on possible internal correlations in the system.

The next section describes how the spectroscopic factor for the  ${}^6\text{He}(0)^+ + 2n$  configuration was deduced. In Section 4.4.2 we show that the assumption of negligible contribution from the  $0p_{1/2}$ -shell contradicts the experimental data.

##### 4.4.1. ${}^6\text{He} + 2n$ configuration in ${}^8\text{He}$ .

The events shown in the  $\vartheta_p$ - $\vartheta_{{}^6\text{He}}$  plot (Fig. 6, panel 2) reveal distinguishing features of the  ${}^6\text{He}$  knockout: correlations  $\vartheta_p$  versus  $\vartheta_{{}^6\text{He}}$ , alignment in the reaction plane, corre-

lations  $\vartheta_p$  versus  $T$  (Fig. 8, panel 2), momentum distribution (Fig. 10, panel 3). However, the shape of  $\frac{d\sigma(t)}{dt}$  for the  ${}^8\text{He}(p, p) {}^6\text{He}$  channel essentially differs from that of  $\frac{d\sigma(t)}{dt}$  for the elastic scattering of a proton on  ${}^6\text{He}$ , as can be seen in Fig. 13. A possible explanation is that the properties of the  ${}^6\text{He}$  cluster inside  ${}^8\text{He}$  differ from those of the free  ${}^6\text{He}$ : i.e., the size of  ${}^6\text{He}$  trapped inside  ${}^8\text{He}$  may be smaller than the size of free  ${}^6\text{He}$ . Note that the nuclear size is directly reflected in the slope and in the magnitude of the scattering cross section.

The general opinion that  ${}^8\text{He}$  consists of an  $\alpha$ -particle surrounded by four neutrons rather than of a  ${}^6\text{He}$ -core surrounded by two neutrons is based on the results of the combined analysis of the interaction and fragmentation cross sections obtained with  ${}^{4,6,8}\text{He}$  beams at 800 MeV/u on a carbon target [7]. This analysis used the Glauber model as described in Ref. [25]. If  ${}^8\text{He}$  has a  ${}^6\text{He} + 2n$  structure, the following relation should be fulfilled

$$\sigma_{-2n}({}^8\text{He}) = \sigma_I({}^8\text{He}) - \sigma_I({}^6\text{He}_{\text{cluster}}), \quad (9)$$

where  $\sigma_{-2n}({}^8\text{He})$  is the two-neutron removal cross section,  $\sigma_I({}^8\text{He})$  is the  ${}^8\text{He}$  interaction cross section, and  $\sigma_I({}^6\text{He}_{\text{cluster}})$  is the interaction cross section of the  ${}^6\text{He}$  cluster. Relation (9) is not fulfilled if  $\sigma_I({}^6\text{He}_{\text{cluster}})$  is replaced by the interaction cross section of free  ${}^6\text{He}$ , as was done in Ref. [7]:  $\sigma_I({}^8\text{He}) - \sigma_I({}^6\text{He}) = 95(9)$  mb while  $\sigma_{-2n}({}^8\text{He}) = 202(17)$  mb. The requirement to satisfy Eq. (9) results in  $\sigma_I({}^6\text{He}_{\text{cluster}}) = 615$  mb instead of 722 mb for free  ${}^6\text{He}$ . A matter radius of the  ${}^6\text{He}$  cluster of  $\langle r^2 \rangle^{1/2} = 1.80$  fm was determined by the Glauber model calculation [26] using this value of  $\sigma_I({}^6\text{He}_{\text{cluster}})$ . This radius is smaller than the one obtained from the analysis of the  ${}^6\text{He}(p, p)$  elastic scattering,  $\langle r^2 \rangle^{1/2} = 2.30(6)$  fm [28].

Assumed that the properties of  ${}^6\text{He}_{\text{cluster}}$  differ from those of free  ${}^6\text{He}$ , the replacement in Eq. (5) of  $(\frac{d\sigma}{dt})_{pc}$  by the elastic-scattering cross section of a proton on a free  ${}^6\text{He}$  is not valid. Consequently, the differential cross section for the elastic scattering on  ${}^6\text{He}_{\text{cluster}}$  was calculated in an eikonal approximation by using the  $(p + \text{cluster})$  optical potential in the “ $t\rho$ ” approximation as described in Ref. [27]. The validity of this approximation was previously checked by reproducing the experimental  ${}^6\text{He}(p, p)$  differential cross section with the two-Gaussian density parameterization ( $R_c = 1.95(10)$  fm,  $R_h = 2.88(27)$  fm with  $\langle r^2 \rangle^{1/2} = 2.30(6)$  fm, as obtained in Ref. [28]). In order to describe the elastic scattering on the  ${}^6\text{He}$  cluster, the density parameters were changed to  $R_c = 1.5$  fm and  $R_h = 2.29$  fm with  $\langle r^2 \rangle^{1/2} = 1.80$  fm. The result of the calculation is shown in Fig. 13, panel 2 by the solid line. The shape of the calculated cross section is close to the experimental  $\frac{d\sigma(t)}{dt}$  thus confirming the QFS mechanism. The spectroscopic factor  $S_{{}^6\text{He}} = 1.3 \pm 0.1$  was derived by the method described above with  $(\frac{d\sigma}{dt})_{pc}$  in Eq. (5) replaced by the calculated  ${}^6\text{He}_{\text{cluster}}(p, p)$  elastic-scattering cross section.

We may therefore conclude that the addition of two neutrons to  ${}^6\text{He}$  results essentially in a shrinking of this nucleus but its shell structure still remains the same. A similar phenomenon was observed in a recent experiment where the charge radii of  ${}^{6,7,8,9}\text{Li}$  were measured by laser spectroscopy [29]. The charge radii decrease gradually with increasing neutron number from 2.51(6) fm for  ${}^6\text{Li}$  to 2.22(9) fm for  ${}^9\text{Li}$ .

#### 4.4.2. ${}^8\text{He}$ with a closed $0p_{\frac{3}{2}}$ shell.

The  ${}^8\text{He}$  wave function (WF), with four neutrons in the  $0p_{\frac{3}{2}}$  shell, can be written in a simple phenomenological form [8] where the essential part of the WF is a Slater determinant constructed from the single-particle WFs

$$\psi_{4n} = \sum_{J=0,2} \mathcal{A}_J \left[ [\psi_{p_{3/2}}(1) \otimes \psi_{p_{3/2}}(2)]_J \otimes [\psi_{p_{3/2}}(3) \otimes \psi_{p_{3/2}}(4)]_J \right]_0, \quad (10)$$

where the coefficients  $\mathcal{A}_J$  determine the weights of the WF component describing the two-neutron subsystem with total spin  $J$ . The  $J = 0$  case corresponds to the  ${}^6\text{He}(0^+) + 2n$  configuration while  $J = 2$  can be described as a configuration with an excited core,  ${}^6\text{He}(2^+) + 2n$ . The obtained weights are  $|\mathcal{A}_0|^2 = 1/6$  and  $|\mathcal{A}_2|^2 = 5/6$ . Thus, the excited  $2^+$  state of  ${}^6\text{He}$  is predominant in the closed-shell  ${}^8\text{He}$  WF [9]. The meaning of the coefficient  $|\mathcal{A}_0|^2$  is equivalent to  $S_{6\text{He}}$  obtained in the present experiment. The discrepancy between such consideration and the result of the present experiment is obvious (see Table 1). Thus, a large weight of the  ${}^6\text{He} + 2n$  structure requires population of the  $0p_{\frac{3}{2}}$  and  $0p_{\frac{1}{2}}$  shells.

The values of  $S_n^\alpha$  and  $S_n^{6\text{He}}$  quoted above also indicate contribution from the  $0p_{\frac{1}{2}}$  shell. Knockout of a neutron from the closed shell in  ${}^8\text{He}$  results in  ${}^7\text{He}$  in its ground state which decays only to  ${}^6\text{He} + n$ . However, a significant yield of  $\alpha$ -particles was observed in the neutron-knockout channel,  $S_n^\alpha = 0.8(1)$ . This observation as well leads to the conclusion that  ${}^8\text{He}$  is not a closed-shell nucleus. In the  $(p_{\frac{3}{2}})^2(p_{\frac{1}{2}})^2$  configuration, a neutron knocked out from the  $0p_{\frac{3}{2}}$  shell results in excited  ${}^7\text{He}$ ,  $(p_{\frac{3}{2}})^1(p_{\frac{1}{2}})^2$ . This state decays via  $\alpha$ -emission. A contribution of the  $(p_{\frac{3}{2}})^2(p_{\frac{1}{2}})^2$  configuration on a level of about 50% can explain the observed yield of  $\alpha$ -particles. A similar result was obtained earlier in studies of the  ${}^8\text{He}$  fragmentation on a carbon target at 227 MeV/u [19].

Thus, the assumption of a doubly magic  ${}^8\text{He}$  nucleus is incompatible with the experimental results. The valence neutrons around  $\alpha$ -core populate both  $0p_{\frac{3}{2}}$  and  $0p_{\frac{1}{2}}$  orbits, and their correlations result in a  ${}^6\text{He}(0^+) + 2n$  structure.

## 5. Summary

Quasi-free scattering of a proton on  ${}^6\text{He}$  and  ${}^8\text{He}$  has been studied in inverse kinematics at relativistic energies. Main results of the analysis of the experimental data are the following:

- The dominance of the QFS mechanism is proven by the independence of the fragment momentum distributions on the beam energy and on the type of the probe particle, by different kinds of correlations between the detected particles in their polar and azimuthal angles and by the dependence of the recoil-proton energy on the emission angle, and by the dependence of the differential cross sections on the momentum transfer.

- An effective method, based on reaction kinematics is proposed to separate different QFS channels.
- For the first time, the internal-momentum distributions of the complex clusters inside  ${}^6\text{He}$  and  ${}^8\text{He}$  have been measured.
- The spectroscopic factors of different cluster configurations in  ${}^8\text{He}$  derived from the experimental data indicate an essential contribution of the  $0p_{\frac{1}{2}}$  shell in its internal structure.
- The quasi-free scattering of protons on the  ${}^6\text{He}$  cluster prevails in the  $(p, p\,{}^6\text{He})$  channel and the observed correlations show the dominant contribution of the  ${}^6\text{He} + 2n$  configuration in the  ${}^8\text{He}$  structure.
- The estimated energy necessary for the removal of the  $\alpha$  cluster from  ${}^8\text{He}$  gives evidence for either a resonance at about 5 MeV in the tetra-neutron system or for strong correlations between valence neutrons in the  ${}^8\text{He}$  wave function.

The investigations described in the present paper show that quasi-free scattering with radioactive beams is a powerful tool providing new perspectives for investigations of the cluster structure of drip-line nuclei. The studies of different QFS channels are important. The  $\alpha$ -knockout reveals mainly the  $\alpha + 4n$  structure, while two channels of the neutron knockout point out the importance of the  $0p_{\frac{1}{2}}$  orbit. The knockout of  ${}^6\text{He}$  directly demonstrates the existence of the  ${}^6\text{He} + 2n$  structure. As perspective, the studies of the nucleon knockout from the  $s$ -shell allow to go beyond the  $\alpha + 4n$  structure and to investigate, for example, how the separation energy of the  $s$ -shell nucleon changes with the increasing number of neutrons.

## Acknowledgements

The authors acknowledge with gratitude useful discussions with Hans Feldmeier, Bjorn Jonson, Jan S. Vaagen, Mikhail Zhukov and their help in the interpretation of the data. This work was partly supported by the RFBR grant No. 04-02-17251.

## References

- [1] G. Jacob, Th.A.J. Maris, Rev. Mod. Phys. 45 (1973) 6;  
G. Jacob, Th.A.J. Maris, Rev. Mod. Phys. 38 (1966) 121.
- [2] O.V. Maxwell, E.D. Cooper, Nucl. Phys. A 513 (1990) 58;  
O.V. Maxwell, E.D. Cooper, Nucl. Phys. A 574 (1994) 819.
- [3] Y. Sakamoto, P. Güer, F. Takéuchi, Phys. Rev. 9 (1974) 2440;  
Y. Sakamoto, P. Güer, F. Takéuchi, Phys. Rev. 11 (1975) 668.
- [4] P.G. Roos, N.S. Chant, A.A. Cowley, D.A. Goldberg, H.D. Holmgren, R. Woody, Phys. Rev. C 15 (1977) 69.
- [5] B. Jonson, Phys. Rep. 389 (2004) 1.
- [6] B.A. Brown, P.G. Hansen, B.M. Sherrill, J.A. Tostevin, Phys. Rev. C 65 (2001) 061601(R).
- [7] I. Tanihata, D. Hirata, T. Kobayashi, S. Shimoura, H. Toki, Phys. Lett. B 289 (1992) 261.
- [8] L.V. Grigorenko, N.B. Shul'gina, M.V. Zhukov, Nucl. Phys. A 607 (1996) 277;  
L.V. Grigorenko, N.B. Shul'gina, M.V. Zhukov, Nucl. Phys. A 614 (1997) 567, Erratum.

- [9] A.A. Korshennikov, E.Yu. Nikolskii, E.A. Kuzmin, A. Ozawa, K. Morimoto, F. Tokanai, R. Kanungo, I. Tanihata, N.K. Timofeyuk, M.S. Golovkov, A.S. Fomichev, A.M. Rodin, M.L. Chelnokov, G.M. Ter-Akopian, W. Mittig, P. Roussel-Chomaz, H. Savajols, E. Pollacco, A.A. Ogloblin, M.V. Zhukov, *Phys. Rev. Lett.* 90 (2003) 082501.
- [10] F.M. Marqués, M. Labiche, N.A. Orr, J.C. Angélique, L. Axelsson, B. Benoit, U.C. Bergmann, M.J.G. Borge, W.N. Catford, S.P.G. Chappell, N.M. Clarke, G. Costa, N. Curtis, A. D'Arrigo, E. de Góes Brennand, F. de Oliveira Santos, O. Dorvaux, G. Fazio, M. Freer, B.R. Fulton, G. Giardina, S. Grévy, D. Guillemaud-Mueller, F. Hanappe, B. Heusch, B. Jonson, C. Le Brun, S. Leenhardt, M. Lewitowicz, M.J. López, K. Markenroth, A.C. Mueller, T. Nilsson, A. Ninane, G. Nyman, I. Piqueras, K. Riisager, M.G. Saint Laurent, F. Sarazin, S.M. Singer, O. Sorlin, L. Stuttgé, *Phys. Rev. C* 65 (2002) 044006.
- [11] F. Aksouh, O.A. Kisselev, A. Bleile, O.V. Bocharev, L.V. Chulkov, D. Cortina-Gil, A.V. Dobrovolsky, P. Egelhof, H. Geissel, M. Hellström, N.B. Isaev, B.G. Komkov, M. Matoš, F.V. Moroz, G. Münzenberg, M. Mutterer, V.A. Mylnikov, S.R. Neumaier, V.N. Pribora, D.M. Seliverstov, L.O. Sergeev, A. Shrivastava, K. Sümmerer, H. Weick, M. Winkler, V.I. Yatsoura, in: 10th Int. Conf. on Nuclear Reaction Mechanisms, Varenna, Villa Monastero, June 9–13, 2003, *Review of the University of Milano, Ricerca Scientifica ed Educazione Permanente, Suppl.* 122 (2003) 157; O.A. Kisselev, et al., *Eur. Phys. J. A* (2005), in press.
- [12] A.W. Stetz, *Phys. Rev. C* 21 (1980) 1979.
- [13] B. Debebe, C.F. Perdrisat, V. Raghunathan, J.M. Cameron, I.J. van Heerden, P. Kitching, R. MacDonald, W.J. McDonald, W.C. Olsen, J. Soukup, H.S. Wilson, H.W. Fearing, C.A. Miller, *Phys. Rev. C* 31 (1985) 1841.
- [14] E.F. Redish, G.J. Stephenson Jr., G.M. Lerner, *Phys. Rev.* 2 (1970) 1665.
- [15] N.S. Chant, P.G. Roos, *Phys. Rev. C* 15 (1977) 57.
- [16] S.B. Treiman, C.N. Yang, *Phys. Rev. Lett.* 8 (1962) 140.
- [17] I.S. Shapiro, V.M. Kolybasov, G.R. August, *Nucl. Phys.* 61 (1965) 353.
- [18] M.V. Zhukov, B.V. Danilin, D.V. Fedorov, J.M. Jang, I.J. Thompson, J.S. Vaagen, *Phys. Rep.* 231 (1993) 151.
- [19] K. Markenroth, M. Meister, B. Eberlein, D. Aleksandrov, T. Aumann, L. Axelsson, T. Baumann, M.J.G. Borge, L.V. Chulkov, W. Dostal, Th.W. Elze, H. Emling, H. Geissel, A. Grünschloss, M. Hellström, J. Holeczek, B. Jonson, J.V. Kratz, R. Kulessa, A. Leistenschneider, I. Mukha, G. Münzenberg, F. Nickel, T. Nilsson, G. Nyman, M. Pfützner, V. Pribora, A. Richter, K. Riisager, C. Scheidenberger, G. Schrieder, H. Simon, J. Stroth, O. Tengblad, M.V. Zhukov, *Nucl. Phys. A* 679 (2001) 462.
- [20] H. Courant, K. Einsweiler, T. Joyce, H. Kagan, Y.I. Makdisi, M.L. Marshak, B. Mossberg, E.A. Peterson, K. Ruddick, T. Walsh, G.J. Igo, R. Talaga, A. Wriekat, R. Klem, *Phys. Rev. C* 19 (1979) 104.
- [21] C.A. Bertulani, H. Sagawa, *Nucl. Phys. A* 588 (1995) 667.
- [22] A.A. Korshennikov, K. Yoshida, D.V. Aleksandrov, N. Aoi, Y. Doki, N. Inabe, M. Fujimaki, T. Kobayashi, H. Kumagai, C.-B. Moon, E.Yu. Nikolskii, M.M. Obuti, A.A. Ogloblin, A. Ozawa, S. Shimoura, T. Suzuki, I. Tanihata, Y. Watanabe, M. Yanokura, *Phys. Lett. B* 316 (1993) 38.
- [23] Y. Suzuki, K. Ikeda, *Phys. Rev. C* 38 (1988) 410.
- [24] M.V. Zhukov, A.A. Korshennikov, M.H. Smedberg, *Phys. Rev. C* 50 (1994) R1.
- [25] Y. Ogawa, K. Yabana, Y. Suzuki, *Nucl. Phys. A* 543 (1992) 722.
- [26] P.J. Karol, *Phys. Rev. C* 11 (1975) 1203.
- [27] L.V. Chulkov, C.A. Bertulani, A.A. Korshennikov, *Nucl. Phys. A* 587 (1995) 291.
- [28] G.D. Alkhazov, A.V. Dobrovolsky, P. Egelhof, H. Geissel, H. Irnich, A.V. Khanzadeev, G.A. Korolev, A.A. Lobodenko, G. Münzenberg, M. Mutterer, S.R. Neumaier, W. Schwabb, D.M. Seliverstov, T. Suzuki, A.A. Vorobyov, *Nucl. Phys. A* 712 (2002) 269.
- [29] G. Ewald, W. Nörtershäuser, A. Dax, S. Gotte, R. Kirchner, H.-J. Kluge, Th. Kühl, R. Sanchez, A. Wojtaszek, B.A. Bushaw, G.W.F. Drake, Z.-C. Yan, C. Zimmermann, *Phys. Rev. Lett.* 93 (2004) 113002.